Journal of Industrial and Engineering Chemistry 153 (2026) 783–796

Contents lists available at ScienceDirect

Journal of Industrial and Engineering Chemistry

journal homepage: www.elsevier.com/locate/jiec

Full Length Article

Exploring the synergistic effects of rGO and MWCNT in NiO-based mesoporous hybrid nanostructures for supercapacitor applications

Govindan Suresh Kumar [a,*], Selvaraj Ranjith Priyan [b], Srinivasan Surendhiran [c], Srinivasan Ramalingam [d,*], Raji Atchudan [e,f,**], Nguyen Van Minh [g,h,***], Mohammed Mujahid Alam [i,j]

[a] Department of Physics, PSG College of Arts & Science, Coimbatore 641014, Tamil Nadu, India
[b] Department of Physics, K.S. Rangasamy College of Arts and Science (Autonomous), Tiruchengode, Namakkal 637215, Tamil Nadu, India
[c] Centre for Nanoscience and Technology, K.S. Rangasamy College of Technology, Tiruchengode, Namakkal 637215, Tamil Nadu, India
[d] Department of Horticulture & Life Science, Yeungnam University, Gyeongsangbuk-do, Gyeongsan 38541, Republic of Korea
[e] Department of Chemistry, Saveetha School of Engineering, Saveetha Institute of Medical and Technical Sciences, Chennai 602105, Tamil Nadu, India
[f] School of Chemical Engineering, Yeungnam University, Gyeongsangbuk-do, Gyeongsan 38541, Republic of Korea
[g] Institute of Research and Development, Duy Tan University, Da Nang 550000, Viet Nam
[h] School of Engineering & Technology, Duy Tan University, Da Nang 550000, Viet Nam
[i] Central Labs, King Khalid University, AlQura'a, P.O. Box 960, Abha, Saudi Arabia
[j] Department of Chemistry, College of Science, King Khalid University, Abha 61421, Saudi Arabia

ARTICLE INFO

Keywords:
NiO
Microwave synthesis
Supercapacitor
r-GO
MWCNTS
Hybrid nanostructure
ASC device

ABSTRACT

In this study, we present a microwave-assisted synthesis to produce NiO, MWCNT@NiO, and rGO@NiO hybrid nanostructures efficiently. Comprehensive characterizations, including XRD, FTIR, FESEM, TEM, EDX, and BET confirmed the formation and structural integrity of MWCNT@NiO and rGO@NiO nanostructures. The nanostructures' electrochemical efficiency was examined in a 2 M KOH electrolyte. The specific capacitance of the rGO@NiO nanostructure is found to be the highest, with 491F/g at a current density of 1 A/g, compared to pure NiO (255F/g) and MWCNT@NiO (370F/g). This greater performance comes from the collaborative properties of the reduced graphene oxide, providing better ion diffusion, charge transfer efficiency, and active surface area with exemplary stability of capacitance of 91 % after 5000 cycles, which is much better cycling and mechanical stability than that of MWCNT@NiO and pure NiO. Furthermore, the electrochemical performance of the rGO@NiO ASC device was assessed using 1 M KOH as the electrolyte throughout a potential range of 0 to 1.2 V. At a current density of 1A/g, the device provided 31.92 Wh/kg energy density and 599.96 W/kg power density. The ASC device demonstrated good charge–discharge behavior, indicating superior capacitance properties and efficient ion transport. Thus, the rGO@NiO hybrid nanostructure can be a potential material for supercapacitor applications.

Introduction

Environmental concerns are pushing the rise in renewable energy sources, emphasizing the need for efficient energy storage solutions. Recent research focuses on improving energy generation and storage for a sustainable future [1]. More efficient energy storage systems have been developed, including fuel cells, supercapacitors and batteries [2–4]. As a result of extremely rapid charge and discharge cycles, long cycle life, more reliable than any other energy-storing system, and high power density, supercapacitors have emerged as promising electrochemical devices for energy storage [5,6]. Since electrode materials are the most crucial constituents in supercapacitor design, they also play an

* Corresponding authors.
** Corresponding author at: Department of Chemistry, Saveetha School of Engineering, Saveetha Institute of Medical and Technical Sciences, Chennai 602105, Tamil Nadu, India.
*** Corresponding author at: Institute of Research and Development, Duy Tan University, Da Nang 550000, Viet Nam.
E-mail addresses: gsureshkumar1986@gmail.com (G.S. Kumar), sribt27@gmail.com (S. Ramalingam), atchudanr@yu.ac.kr (R. Atchudan), nguyenvanminh15@duytan.edu.vn (N.V. Minh).

https://doi.org/10.1016/j.jiec.2025.09.001
Received 7 April 2025; Received in revised form 7 August 2025; Accepted 1 September 2025
Available online 2 September 2025

important role in affecting the performance and, therefore, in determining the supercapacitor's energy storage capacity and power delivery [7,8]. In recent years, the development of advanced electrode materials with high specific capacitance, excellent rate capability, and long cycle stability has gained significant attention in the field of electrochemical energy storage. Moreover, achieving high energy density while maintaining rate performance and durability remains a considerable challenge. This led to many works focusing on developing new electrode materials that depict enhanced specific capacitances based on efficient charge storage mechanisms such as pseudocapacitance and interfacial redox activity. Nanostructured transition metal oxides, conducting polymers, and hybrid materials with carbonaceous supports have recently been in the spotlight for investigation. MXene/polymer hybrid materials have shown extraordinary performances for fast charge transport flexible AC-filtering electrochemical capacitors [9]. On the other hand, analysing molecular-level aspects for the surface redox mechanism of oxidized black phosphorus nanosheets demonstrated nearly in ideal pseudocapacitive behaviours, with 99 % capacitive contribution at 2,000 mV s^{-1} and much better long-term cycling stability [10]. These recent strategies highlight the crucial role of interfacial engineering, heterostructure design, and nanostructuring for fabricating advanced next-generation supercapacitor electrodes.

Transition metal oxides, such as NiO, Co_3O_4, and MnO_2, have been extensively explored due to their multiple redox states and high theoretical capacitance. Among different transition metal oxides, NiO exhibits cost-effectiveness, excellent electrical conductivity, and the impressive versatility in oxidation states, which render them valid candidates for supercapacitor electrodes [11–13]. Additionally, various synthesis methods allow for tailored morphologies that optimize performance [14–18]. Poor electrical conductivity is always limiting their practical performance. To solve this problem, hybridization with carbon nanomaterials emerges as a promising strategy. Metal oxides and carbon-based composites make good supercapacitor electrodes due to metal oxides' high redox activity, which combines with the superior conductivity and surface area exhibited by carbon materials to generate better capacitance, rate performance, and long-term stability [19–23]. Hence, carbon material integration with NiO considerably raises electrochemical properties, reliability, and the cost effectiveness of supercapacitor electrodes [24,25]. Xu et al. reported hydrothermal synthesis of NiO/rGO nanocomposites and found these to have higher specific capacitance than pure NiO because of conductivity and electrochemical efficiency improvements [26]. Gund et al. prepared a flexible electrode using NiO/MWCNT nanocomposite, achieving the highest specific capacitance compared to pure NiO [27]. The enhanced electrical mobility and remarkable transport of carriers of rGO and MWCNTs provide them with suitable materials for supercapacitors, while their combined structures with metal oxides enhance electrochemical properties attributed to the collaborative effects of the different components [28,29].

Different methods, including hydrothermal process, chemical vapour deposition, microwave process and sol–gel methods, have been widely used to prepare the hybrid nanostructures [30–34]. Nevertheless, the microwave-assisted method is a facile and rapid approach to preparing nanoparticles with controlled morphologies. This technique has been found to enhance reaction kinetics, thus speeding up the synthesis of hybrid nanostructures [35]. The microwave-assisted synthesis benefits from fast synthesis, enhanced phase purity, even distribution of particle sizes, and morphology control [36]. Polyethylene glycol (PEG) further aids in directing the synthesis toward specific nanostructures and enhances surface properties due to its adjustable molecular weight, flexible structure, and structural flexibility [37]. It is recognized for its surfactant and stabilising properties, which assist in the fine formation of MWCNT@NiO and rGO@NiO hybrid nanostructures with enhanced electrochemical performance. In this work, we propose a facile method for rapid microwave synthesis of rGO@NiO and MWCNT@NiO hybrid nanostructures. These hybrids provide a synergistic effect that combines the pseudocapacitance of NiO with the electrical conductivity and surface area of the carbon-based materials. This synergistic action effectively promotes charge transport, ion diffusion, and cycling stability. Among all the synthesised materials, rGO@NiO exhibits outstanding electrochemical performance compared to NiO and MWCNT@NiO alone and hence represents a quite interesting step toward developing high-performance electrode materials for future-generation supercapacitors.

Experimental procedure

Synthesis

NiO-based hybrid nanostructures were prepared using a very simple microwave-assisted technique. $Ni(NO_3)_2{\cdot}6H_2O$ was dissolved in deionized water (100 ml) and then 0.05 M PEG was added to this by vigorous mixing at room temperature. The pH of the reaction mixture was increased to 11 using ammonia to get a precipitate. The obtained precipitation was then irradiated with 700 W microwave power for 10 min. After cooling, ageing was performed for 24 h. Then, the precipitate was obtained from the reaction mixture through successive ethanol washes and centrifugation. Then, it was subsequently dried at 120 °C for 8 h. Finally, the dried product was heated at 400 °C in a muffle furnace to enhance crystallinity and achieve the desired NiO nanostructure. A similar procedure was employed to produce rGO@NiO and MWCNT@NiO hybrid nanostructures by adding 0.1 g of rGO and MWCNTs into the reaction mixture during the precipitation stage. Accordingly, the three samples were prepared and labelled as NiO, rGO@NiO, and MWCNT@NiO nanostructures for reference throughout the study. The schematic of the synthesis of rGO@NiO and MWCNT@NiO hybrid nanostructures is shown in Fig. 1.

Characterization

The structural analysis was conducted using Cu Kα X-ray source in the Rigaku MiniFlex diffractometer. Functional groups in the prepared samples were analyzed through a Nicolet Summit FTIR spectrometer. Particle size and shape were investigated via FESEM (Carl Zeiss- Sigma 300 & Carl Zeiss SUPRA 55) and TEM (FEI Tecnai G220 S-TWIN TEM). SmartEDX system integrated in ZEISS Sigma 300 FESEM system was used to analyze the elemental composition of the samples via Energy Dispersive X-ray Spectroscopy (EDX). N_2 adsorption/desorption profile were analyzed via Quantachrome Instruments, Autosorb IQ series and the BJH method was employed to determine the pore characteristics [38].

Electrochemical test

Supercapacitance characteristics of the prepared samples was investigated using a CH Instruments electrochemical tester with a three-electrode. Working electrodes were prepared by slurry-coating 80 wt% synthesized composites, 15 wt% conductive carbon, and 5 wt% PTFE in 1-methyl-2-pyrrolidinone, applied onto nickel foam (1 × 1 cm^2) and dehydrated for 12 h at 80 °C. Working electrodes with NiO, MWCNT@NiO, and rGO@NiO were analyzed in 2 M KOH using Ag/AgCl and Pt electrodes.

The asymmetric supercapacitor (ASC) device was fabricated by combining the anode and cathode with active material coated in a 1:5 ratio on an alumina substrate. Both electrodes were depositing equal surface areas (1 × 1 cm^2) of the rGO@NiO hybrid nanostructure. A Whatman filter paper pre-soaked in 1 M KOH electrolyte was employed as a separator to avoid direct contact between the electrodes while enabling ionic conduction. The fabricated ASC device was then tightly sealed with insulating tape to preserve structural integrity and reduce electrolyte evaporation.

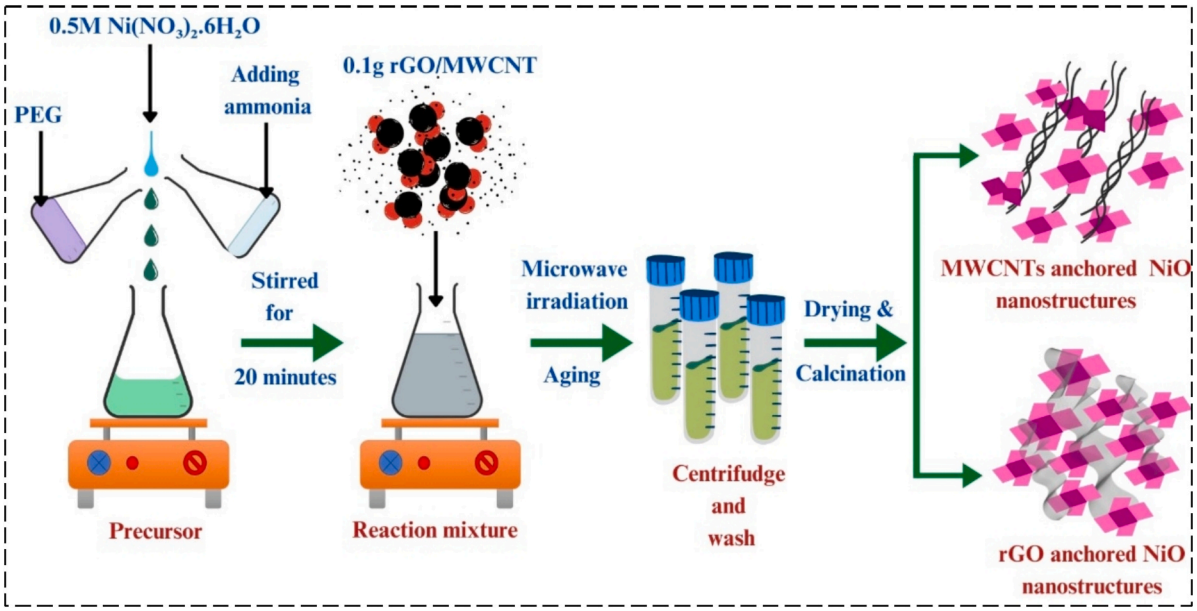

Fig. 1. The steps involved in the preparation of rGO@NiO, and MWCNT@NiO hybrid nanostructures.

Results and discussion

Fig. 2 depicts the XRD patterns of NiO, MWCNT@NiO, and rGO@NiO hybrid nanostructures, revealed peaks at 2θ = 36.96° (111), 43.08° (200), 62.56° (220), 74.92° (311), and 78.72° (222) which were well matched with standard XRD data (JCPDS card No. 47-1049) of NiO having fcc structure [26,39,40]. In the XRD pattern of rGO@NiO and MWCNT@NiO nanostructures, a prominent carbon hump was observed compared to pure NiO, confirming the successful incorporation of rGO and MWCNT into the NiO matrix. The absence of other peaks confirms the purity of the prepared samples. Due to enhanced crystallinity or preferred orientation of NiO with MWCNT, NiO peaks in the MWCNT@NiO composite are of much higher intensity than those of rGO@NiO. The tubular structure of MWCNTs offers a more uniform and stable platform for NiO nucleation and growth, yielding sharper and more intense diffraction peaks. On the contrary, the wrinkled and flexible nature of rGO may be responsible for less ordered NiO crystallites, thus reducing the intensity of peaks in XRD. Fig. 2(d) and (e) shows the XRD patterns of pure rGO and MWCNTs, revealing broad diffraction humps near 2θ ≈ 25°, which are indicative of the typical (002) diffraction of rGO and MWCNTs, reflecting their less ordered or amorphous carbon structures.

Fig. 3 shows the FTIR vibrational spectrum of pure NiO, MWCNT@NiO, and rGO@NiO hybrid nanostructures, revealing various peaks representing their functional groups' vibrations. The peak at 574 cm^{-1} in pure NiO is attributed to stretching Ni-O vibrations, showing formation of NiO. The wide band located at 3445 cm^{-1} owing to stretching O–H vibrations, indicates the presence of H_2O molecules [41]. The oxygen-containing functional groups on the MWCNT framework are identified by the peaks 385 cm^{-1} and 1108 cm^{-1} in the MWCNT@NiO spectra, which correspond to C–O and C=O stretching vibrations. In MWCNTs, the asymmetric and symmetrical extension vibrations of C–H bonds are characterized by the peaks at 2926 cm^{-1} and 2850 cm^{-1} [42]. Additionally, the peak at 1640 cm^{-1} in the rGO@NiO spectra revealed C=O stretching vibration. The peaks at 1385 cm^{-1} and 1108 cm^{-1} indicate the C-O and C-O-C stretching vibrations of rGO in the composite structure [43]. The observed carbon-related peaks demonstrate a strong interaction between NiO and rGO, resulting in a

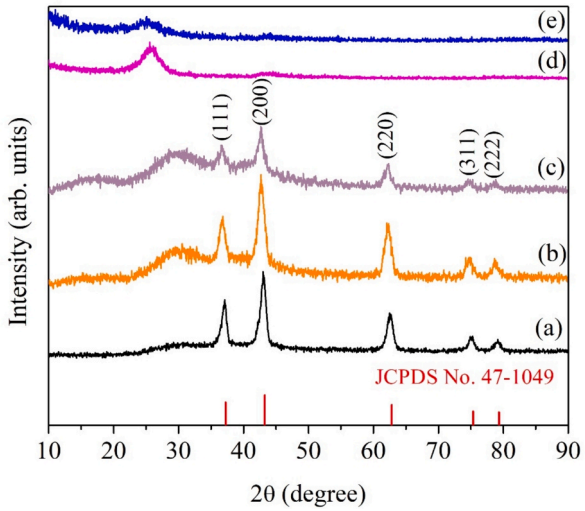

Fig. 2. XRD pattern of (a) NiO, (b) MWCNT@NiO, (c) rGO@NiO hybrid nanostructures, (d) MWCNT, (e) rGO.

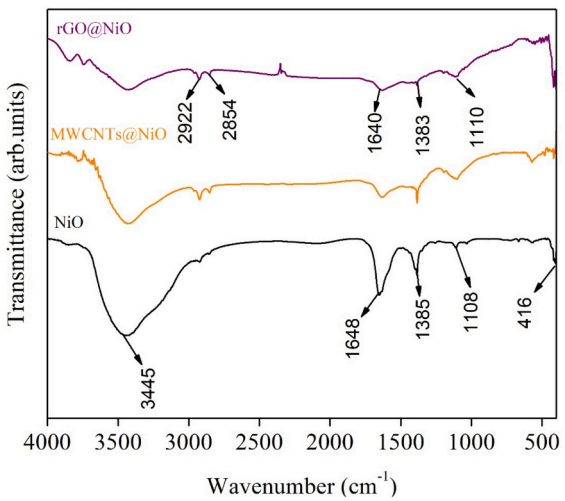

Fig. 3. FTIR vibrational spectrum of NiO, MWCNT@NiO, and rGO@NiO hybrid nanostructures.

well-integrated composite structure.

The Raman spectrum of pure NiO shown in Fig. 4(a) has peaks around 300–600 cm^{-1} and 1050–1100 cm^{-1}, indicating one-phonon and two-phonon LO modes owing to Ni-O vibrations in the fcc lattice. In the NiO-rGO composite (Fig. 4(b)), additional peaks at 1350 cm^{-1} (D band) and 1580 cm^{-1} (G band) were observed, revealing disordered and graphitic carbon structures of reduced graphene oxide. For NiO-MWCNT composite (Fig. 4(c)), along with NiO vibrations, D and G bands coupled with a sharp 2D band (~2700 cm^{-1}) were observed, corroborating the presence of MWCNTs. The rGO or MWCNT imparts strong carbon features and slightly shifts NiO peaks because of the interfacial action and associated strain on NiO lattice, indicating the formation of a hybrid successfully.

Fig. 5 shows FESEM pictures of NiO, rGO@NiO, and MWCNT@NiO hybrid 2D nanostructures. Fig. 5(a) and (b) show the flake-like morphology of pure NiO, highly agglomerated in nature, and uniform in shape and size. The NiO nanoflakes possess a distinct and porous architecture, suitable for maximising the surface area and enhancing the electrochemical performance. FESEM pictures of MWCNT@NiO nanostructures, shown in Fig. 5(c) and (d), clearly demonstrate that MWCNTs are well integrated with NiO nanoflakes to form a hybrid composite. MWCNTs help impart mechanical stability to NiO nanoflakes, preventing them from agglomerating and maintaining their high surface area. FESEM images of rGO@NiO nanostructure at different magnifications (Fig. 5e) and f)) revealed strong integration of rGO and NiO, corroborating the hybrid composite formations.

Fig. 6(a) and (b) shows TEM images revealed pure NiO has a flakes-like morphology with a mesoporous structure. The microwave treatment is a powerful way to improve and speed up the growth of NiO nanostructures by quickly heating reaction mixture, ensuring uniform nucleation and controlled growth of crystals. Hence well-defined nanoflakes with size uniformity were achieved [44]. As expected, the EDS spectrum shown in Fig. 6(c) revealed Ni and O as the most abundant components. Ni and O compositions were 78.85 wt% and 21.15 wt%, respectively. Fig. 6(d) and (e) revealed the elemental mapping indicates that O and Ni have a uniform distribution throughout the nanostructures.

Fig. 7(a) and (b) shows the TEM analysis of MWCNT@NiO nanostructure at different magnifications. MWCNTs can be distinctly seen mixed with NiO, forming a strong interfacial contact. The EDS spectrum in Fig. 7(c) showed the presence of C, O, and Ni at 9.81 wt%, 27.56 wt%, and 62.63 wt%, respectively, proving the successful formation of the nanostructure. Elemental mapping images are shown in Fig. 7(d–f) revealed the uniform distribution of oxygen, nickel, and carbon. This indicates that MWCNT is firmly integrated with the NiO matrix.

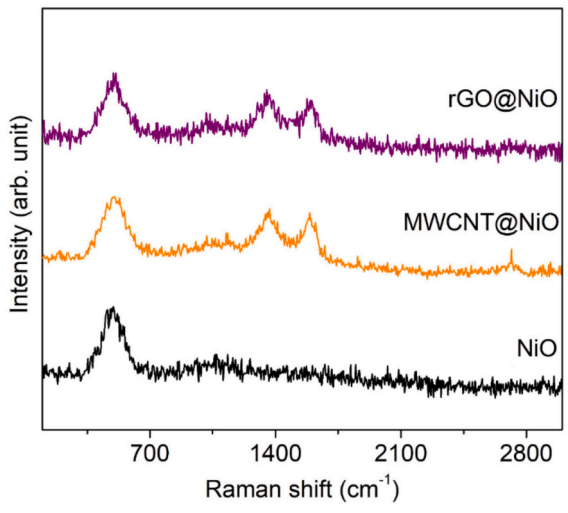

Fig. 4. Raman spectrum of NiO, MWCNT@NiO, and rGO@NiO hybrid nanostructures.

The TEM images of the rGO@NiO nanostructure is shown in Fig. 8(a) and (b). It revealed the integration of rGO sheets with NiO nanoflakes. The EDS spectra confirm the occurrence of C, O, and Ni with 11.82 wt%, 22.14 wt%, and 66.04 wt% composition (Fig. 8c). Fig. 8(d–f) demonstrates elemental mapping images of a uniform distribution of C, O, and Ni, indicating that rGO and NiO are dispersed throughout the sample. This uniformity is essential for enhancing the electrochemical functionalities of the nanostructure, as it enables efficient electron transport and provides a large surface area for energy storage applications, making it an attractive possibility for supercapacitors.

Specific surface area (SSA) and pore characteristics are essential characteristics of the material for making supercapacitor electrode [45,46]. The N_2 adsorption–desorption and pore characteristics curve in Fig. 9 revealed the textural properties of pure NiO, MWCNTs@NiO and rGO@NiO nanostructures. N_2 adsorption–desorption isotherm of all samples exhibits Type IV characteristics with a hysteresis curve, indicating the presence of mesoporous structures in all samples. Pure NiO (Fig. 9a) shows adsorption potential in the moderate range. Adding MWCNTs (Fig. 9c) enhances the surface area and thus improves the adsorption behaviour. A higher adsorption capacity is exhibited by the rGO@NiO hybrid nanostructure (Fig. 9e), suggesting better porosity and structural integration. The pore size distribution plots (Fig. 9b, d, and f) confirm mesoporosity, with the dominant pores with diameters of less than 20 nm in NiO and MWCNT@NiO. On the other hand, rGO@NiO has a broader pore size distribution that reaches 40 nm. These observations highlight the importance of carbon-based materials in improving the textural and adsorption characteristics of NiO. The findings indicate that the rGO@NiO nanostructures exhibit sufficiently large surface area, which is essential for appropriate, quick transport pathways for electrolyte ions that greatly enhance the capacitive properties of the nanostructures [47,48]. Table 1 shows the SSA and pore diameters of the prepared samples.

Fig. 10(a) compares CV curves for the three electrodes at 100 mV/s. The redox peaks correspond to the Ni(II)/Ni(III) redox transitions in KOH solution [49]. The CV measurements also observed a small contribution from the nickel foam. Among the tested electrodes, the rGO@NiO nanostructure showed the largest curve area, indicating the highest specific capacitance compared to MWCNT@NiO and pure NiO electrodes. Fig. 10(b–d) displays the CV curves of pure NiO, MWCNT@NiO, and rGO@NiO nanostructures. The rectangular CV curve with a small redox peak results from combining a double electric layer and pseudocapacitance characteristics [50]. The rGO@NiO nanostructure shows a large enclosed area in CV curves, revealing its good capacitance [51]. The high efficiency of rGO@NiO owing to the large surface area and good conductivity of rGO. These features allow for effective ion diffusion and charge transfer. The extensive surface area of rGO provides multiple active sites for redox reactions, which boosts its specific capacitance. NiO delivers pseudocapacitance through reversible Faradaic redox reactions at the electrode–electrolyte interface, mainly involving the Ni^{2+}/Ni^{3+} redox couple:

$$NiO + OH^- \leftrightarrow NiOOH + e^-$$

This reaction occurs near alkaline electrolytes (KOH) surface, leading to high specific capacitance. At the same time, rGO and MWCNTs add electric double-layer capacitance (EDLC) by physically adsorbing ions on their high-surface-area conductive surfaces, which is explained by the non-Faradaic mechanism. Further, a capacitance contribution analysis was conducted to differentiate between EDLC and pseudocapacitive behaviour. This was performed using two approaches. First, the power-law relationship between peak current (i) and scan rate (v), expressed as $i = av^b$, was used to determine the b-value from the slope of the log*(i) vs.* log*(v)* plot [52]. A b-value close to 1 indicates a capacitive process, while a value near 0.5 suggests diffusion-controlled behavior. log*(i) vs.* log*(v)* plot for NiO, MWCNT@NiO, and rGO@NiO electrodes is

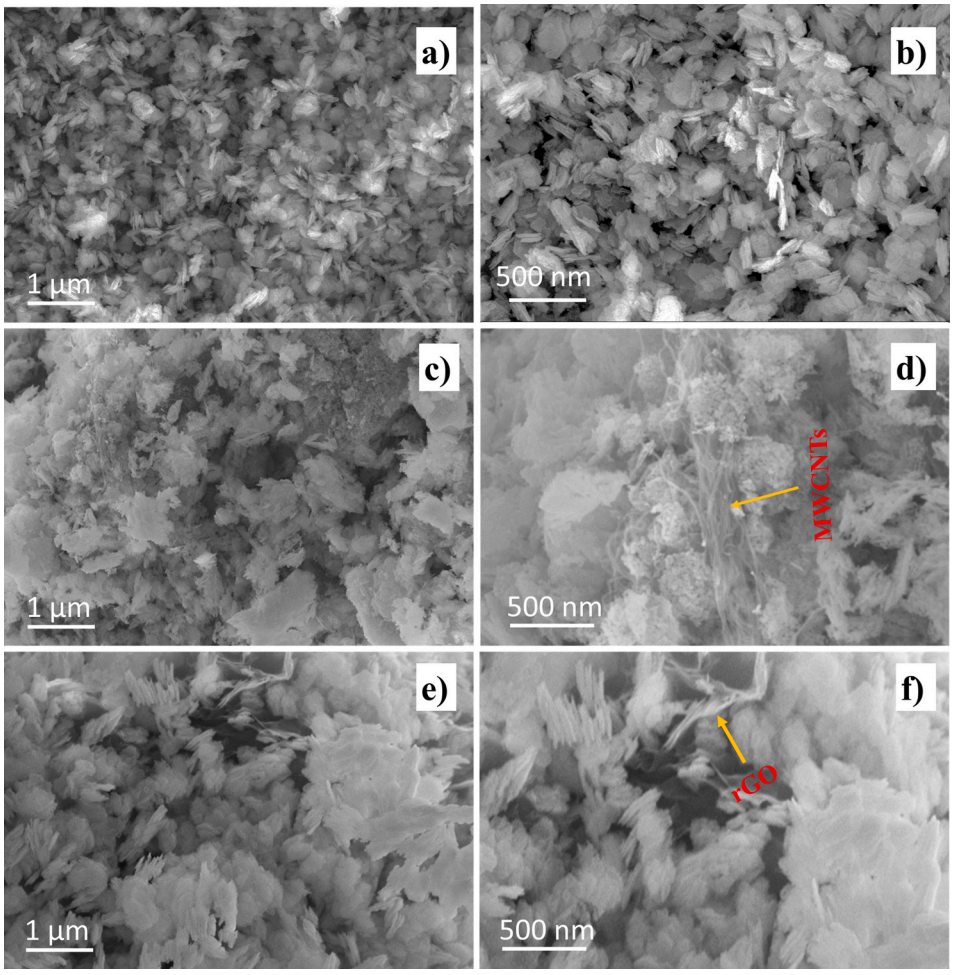

Fig. 5. FESEM pictures of the (a & b) pure NiO, (c & d) MWCNT@NiO, (e & f) rGO@NiO hybrid nanostructures.

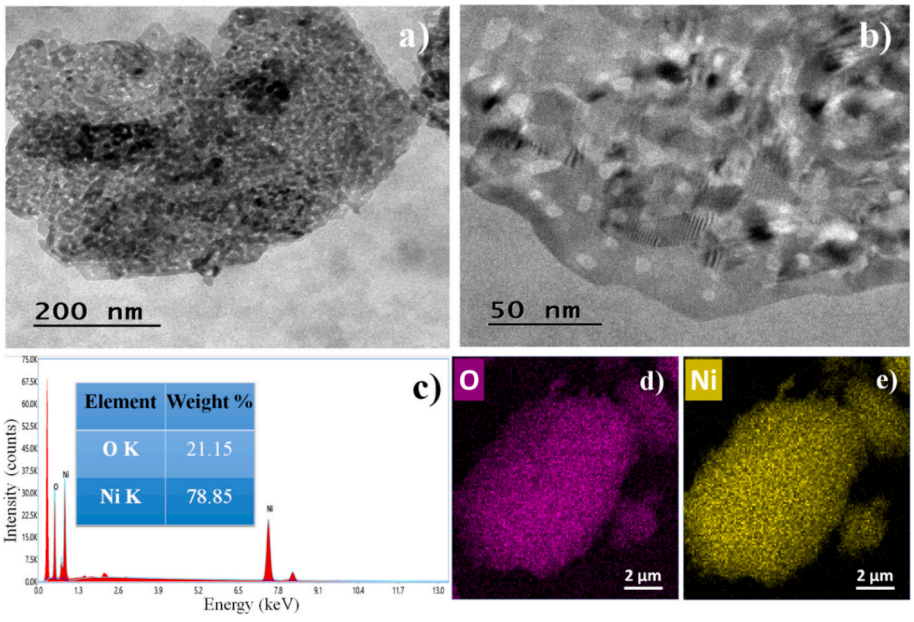

Fig. 6. (a & b) TEM images, (c) EDS spectra, (d & e) elemental imaging of pure NiO.

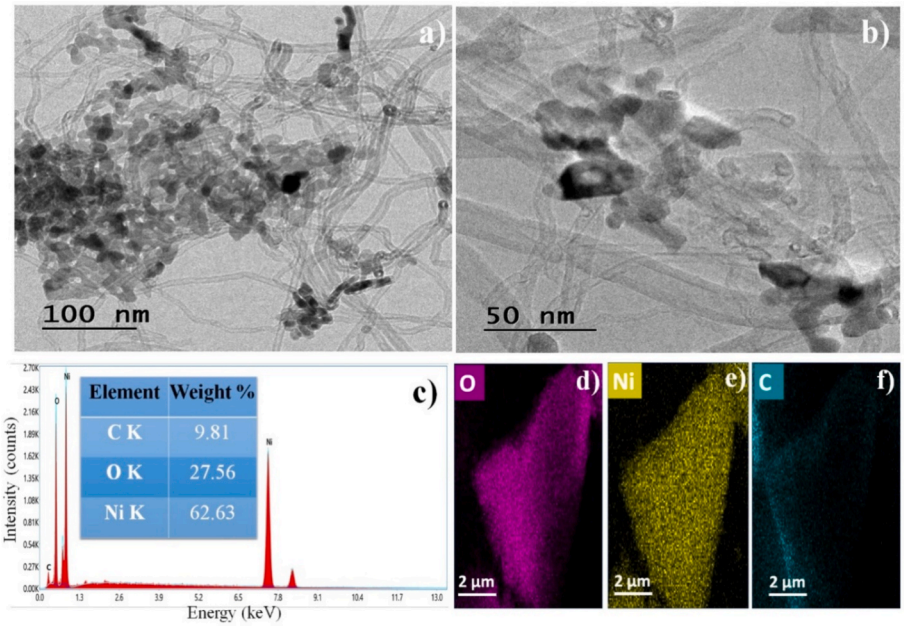

Fig. 7. (a & b) TEM images, (c) EDS spectra, (d–f) elemental imaging of MWCNT@NiO nanostructure.

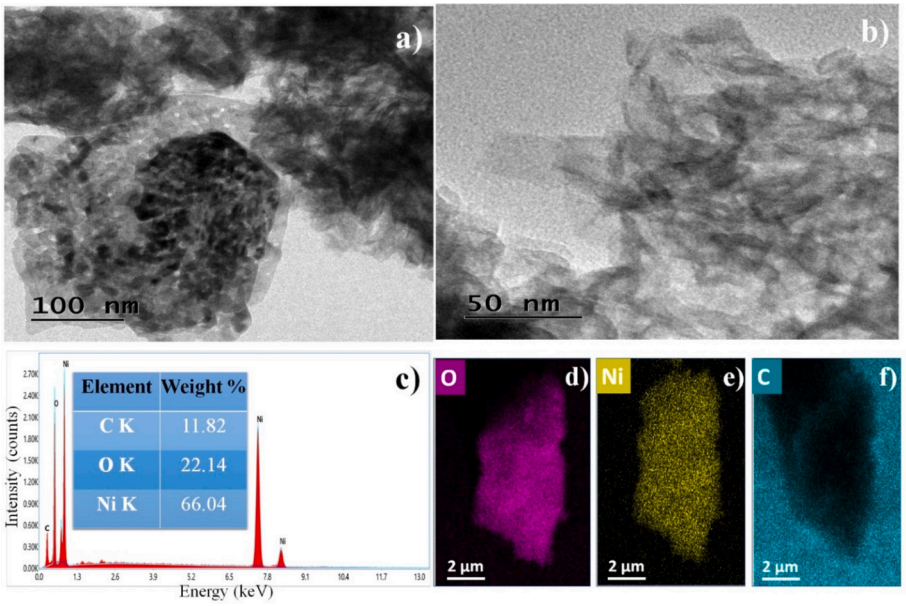

Fig. 8. (a & b) TEM images, (c) EDS spectra, (d–f) elemental imaging of rGO@NiO nanostructure.

shown Fig. S1. The b-values for the NiO, MWCNT@NiO, and rGO@NiO electrodes are 0.7418, 0.6755, and 0.6374, respectively. This indicates a mixed charge storage mechanism in all three systems. Since these b-values fall between 0.5 and 1.0, they suggest that the electrochemical behavior comes from a mix of capacitive (surface-controlled) and diffusion-controlled (faradaic) processes. The NiO electrode shows the highest b-value at 0.7418, which means it has a greater contribution from surface-controlled pseudocapacitive behaviour. In contrast, the b-values for MWCNT@NiO at 0.6755 and rGO@NiO at 0.6374 are slightly lower. This indicates a stronger effect of diffusion-controlled redox reactions, likely due to the improved porosity and conductivity from the MWCNT and rGO networks. These values confirm that adding carbon materials helps ion diffusion and electron transport and brings more diffusion-limited contributions to the overall charge storage process. Second, Dunn's method was applied using the equation $i(V) = k_1 v + k_1 v^{\frac{1}{2}}$, where $k_1 v$ corresponds to the capacitive contribution and $k_1 v^{\frac{1}{2}}$, to the diffusion-controlled contribution [53,54]. The Dunn's method analysis shown in Fig. S2 differentiates the charge storage mechanisms of NiO, MWCNT@NiO, and rGO@NiO electrodes. It offers essential insights into how these electrodes store charge at different scan rates. For the pure NiO electrode, the current response at low scan rates, like 5 and 20 mV/s, is mainly controlled by diffusion, contributing about 82 % and 69 %, respectively. This indicates battery-type behaviour driven by Faradaic redox processes that involve ion intercalation and bulk diffusion. As the scan rate increases, the capacitive contribution becomes more significant. At 100 mV/s, the contributions from both capacitive and diffusion-controlled mechanisms are nearly equal. At 200 mV/s, the capacitive behaviour takes over, accounting for about 58 %. This change indicates that NiO shows a mixed charge storage mechanism: diffusion-controlled at low rates and capacitive at high rates. This makes it a

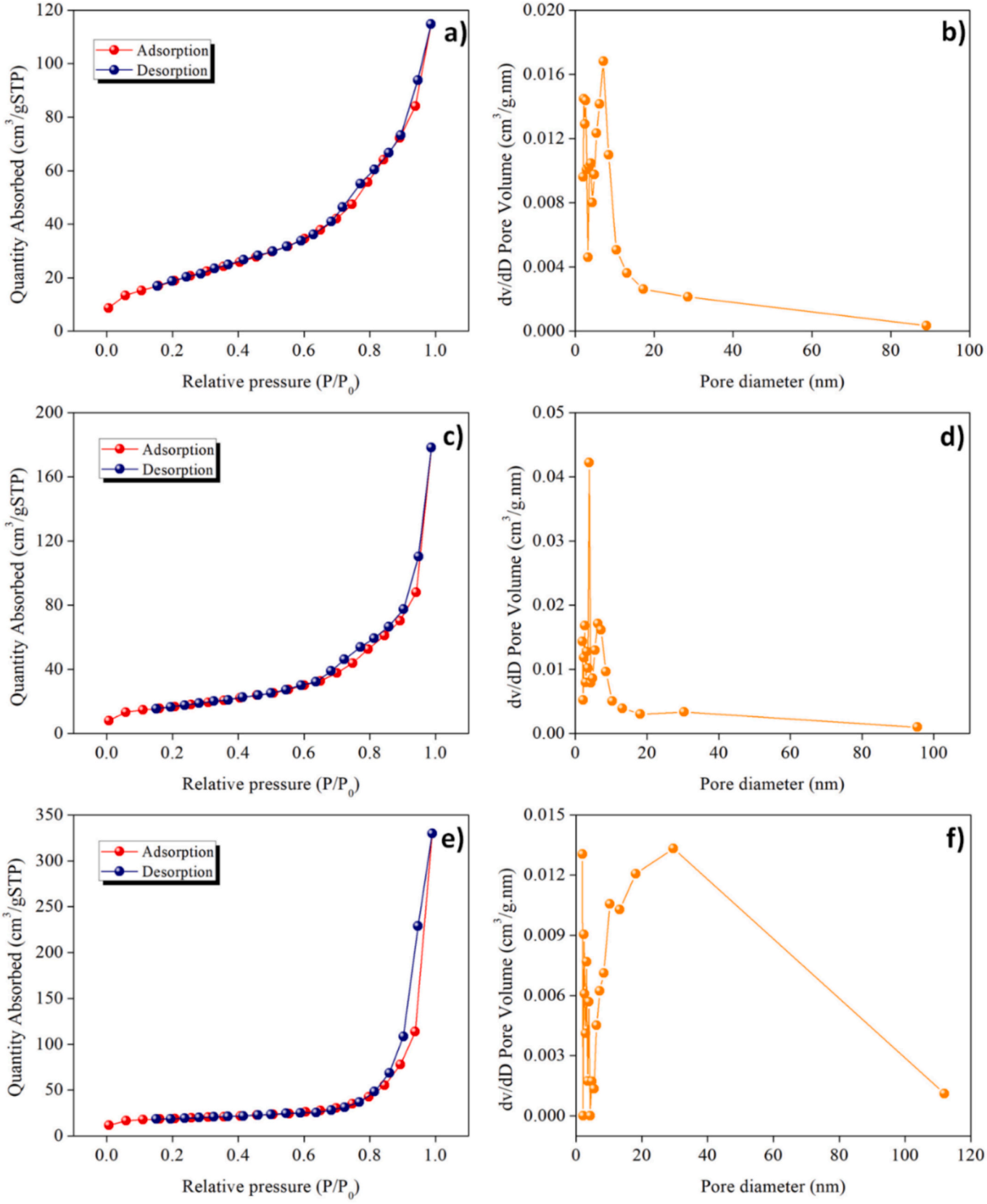

Fig. 9. The N_2 adsorption–desorption profile and pore characteristics of (a & b) pure NiO, (c & d) MWCNT@NiO, (e & f) rGO@NiO hybrid nanostructures.

Table 1
The SSA and pore characteristics of the prepared hybrid nanostructures.

Materials	SSA ($m^2\ g^{-1}$)	Pore size (nm)	Pore volume ($cm^3 g^{-1}$)
Pure NiO	91.935	7.095	0.196
MWCNT@NiO	103.034	3.864	0.316
rGO@NiO	114.933	9.572	0.559

potential electrode material for energy storage. In contrast, the MWCNTs@NiO electrode shows strong capacitive dominance at all scan rates. Even at 5 mV/s, the capacitive contribution is notable at around 54 %, quickly rising to about 88 % at 200 mV/s. This strong capacitive behaviour is due MWCNTs, which improve electrical conductivity, increase the electrochemically active surface area, and enable fast transport of electrons and ions. These characteristics make MWCNTs@NiO a good candidate for supercapacitor applications, especially for high-power and rapid cycling tasks. The rGO@NiO electrode displays an intermediate behaviour, transitioning smoothly from diffusion-dominated to capacitive-dominated mechanisms as the scan rate increases. At 5 mV/s, diffusion controls the contribution at around 79 %, showing strong Faradaic interactions. The capacitive component gradually rises with the scan rate, reaching about 63 % at 200 mV/s. This trend demonstrates how reduced graphene oxide (rGO) improves surface-controlled processes. rGO enhances charge transfer kinetics and helps accommodate quick ion diffusion, thereby improving capacitive performance. These findings show how combining NiO with carbon-based nanostructures like MWCNTs and rGO can effectively adjust the charge storage mechanism. While pure NiO is better for energy-dense systems due to its battery-like behavior, MWCNTs@NiO offers excellent rate performance suited for power-intensive applications. rGO@NiO presents a balanced hybrid profile, making it a strong candidate for next-generation supercapacitors requiring high energy and power densities.

Fig. 11(a) shows the GCD profile of the prepared sample as the electrode at 3 A/g. The rGO@NiO nanostructure lasts longer during discharge than pure NiO and MWCNT@NiO, indicating better energy storage capability. A larger surface area of rGO allows more ion adsorption, significantly boosting its capacitive performance [55]. The GCD curves for pure NiO, MWCNT@NiO, and rGO@NiO at different current densities are illustrated in Fig. 11(b–d). As current density increases, the discharge times for all nanostructures decrease, a typical behaviour for supercapacitor materials [56,57]. The electrode's specific capacitance (C, F/g) was estimated using the equation,

$$C = I.\Delta t/m.\Delta V \quad (1)$$

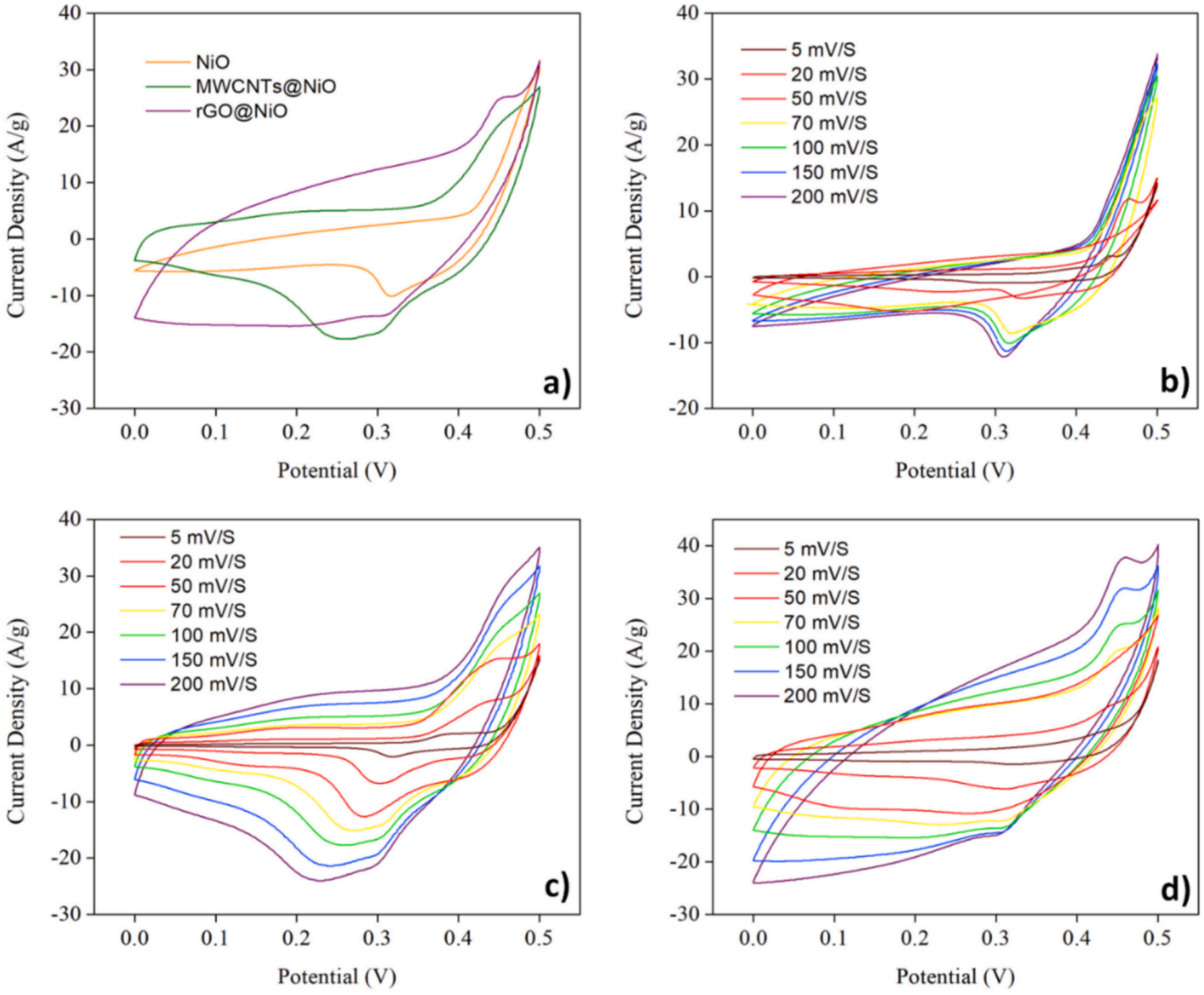

Fig. 10. (a) Comparative CV curves of the electrodes recorded at a scan rate of 100 mV/s. CV curves of (b) pure NiO, (c) MWCNT@NiO, and (d) rGO@NiO hybrid nanostructures.

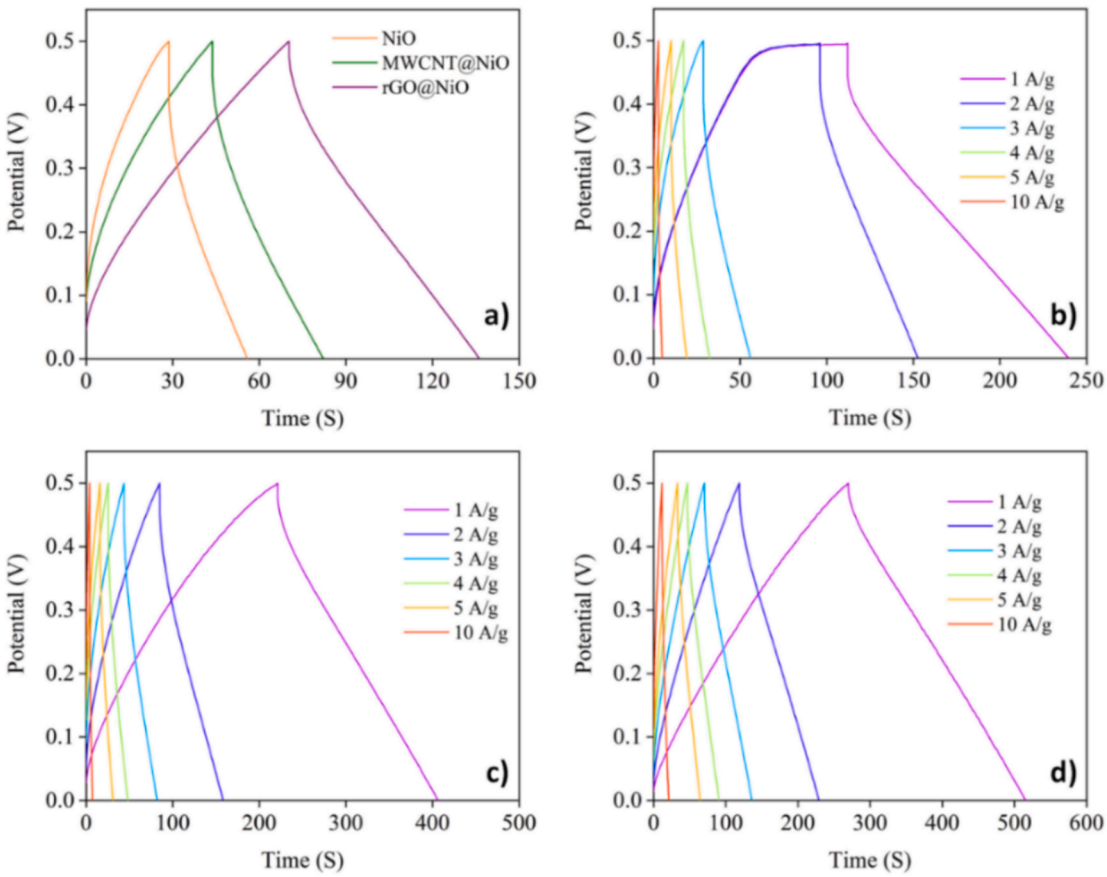

Fig. 11. (a) Comparative GCD profiles of the prepared samples as a electrode at 3 A/g. GCD profiles at various current densities for (b) NiO, (c) MWCNT@NiO, and (d) rGO@NiO hybrid nanostructures.

where I is the impressed current, m is the mass of each electrode, Δt is the scan time interval, and ΔV is the voltage range of each scan.

The specific capacitance of pure NiO, MWCNT@NiO, and rGO@NiO hybrid nanostructures is shown in Fig. 12(a) and Table 2. At a current density of 1 A/g, the rGO@NiO electrode has a specific capacitance of 491F/g. This is higher than MWCNT@NiO (370F/g) and NiO (255F/g). Nickel oxide undergoes fast redox reactions and can store charge. NiO nanoparticles improve the accessibility of electrolyte ions in rGO@NiO electrodes. This reduces ion diffusion resistance and migration barriers by improving the interfacial contact through interaction with rGO [58]. The potential of rGO to provide a higher surface area increases adequate charge storage, which boosts performance [59]. Additionally, the better electrical conductivity of rGO improves electron transport and overall electrochemical performance. Moreover, MWCNT@NiO has a higher specific capacitance than pure NiO due to the conductivity of the MWCNTs, which enhances the overall electrochemical properties [60]. However, the rGO@NiO electrode still has the highest capacitance values, showing its significance in improving supercapacitor performance.

Fig. 12(b) shows the capacitance retention which was calculated using below equation:

$$Capacitance Retention(\%) = 100 \times \frac{\text{Final Capacitance}}{\text{Initial Capacitance}} \quad (2)$$

The capacity retained for the rGO@NiO nanostructure electrode was 91 %. In contrast, the MWCNT@NiO and pure NiO nanostructure electrodes showed 84 % and 79 % retention, respectively. The rGO@NiO nanostructure proved very stable for long-term energy storage applications, as demonstrated by its high specific capacitance even after 5000 GCD cycles. The better retention is due to the strong interaction between rGO and NiO, which effectively absorbs volume changes during repeated charge and discharge cycles. This helps keep the electrode's structure intact. Table 3 compares the specific capacitance of the samples in this study with previously reported results.

The EIS spectra cover the range from 1 MHz to 0.1 Hz is shown in Fig. 12(c,d). The semi-circle at higher frequencies reflects the charge transfer resistance (Rct1). This information helps us understand the electron transfer limitations between the platinum counter electrode and the electrolyte. Next, the second semi-circle appears in the mid-frequency section, representing the charge transport resistance across the sample and electrolyte (Rct2). This allows us to consider how charge carriers move through the electrode material. In the Nyquist plot, the axis intersects at the equivalent series resistance (Rs). Rs includes the series resistance from the electrolyte, the electrodes' resistance, and the intrinsic electrical contacts. The semi-circle in the Nyquist plot measures the charge transfer resistance (Rct), which influences how fast electrochemical reactions occur. These frequency limits extend into the low-frequency area, showing linear growth in the Nyquist plot, which relates to the Warburg Impedance (Zw). Warburg impedance indicates the resistance to mass diffusion of ions within the electrode pores and electrolyte. A steeper slope in this region generally suggests improved ion diffusion, leading to better electrochemical performance. The Rs values for pure NiO, MWCNT@NiO, and rGO@NiO are 0.45 Ω, 0.77 Ω, and 0.98 Ω, respectively. rGO@NiO has a lower Rs than both MWCNT@NiO and pure NiO, indicating better conductivity and ion transport within the electrolyte. It has good electrochemical conductivity and low internal resistance, resulting in a fast charge transmission rate. Integrating reduced graphene oxide in the NiO matrix provides two benefits. It lowers charge resistance, which boosts the material's electrochemical performance [69,70]. It also increases the overall charge

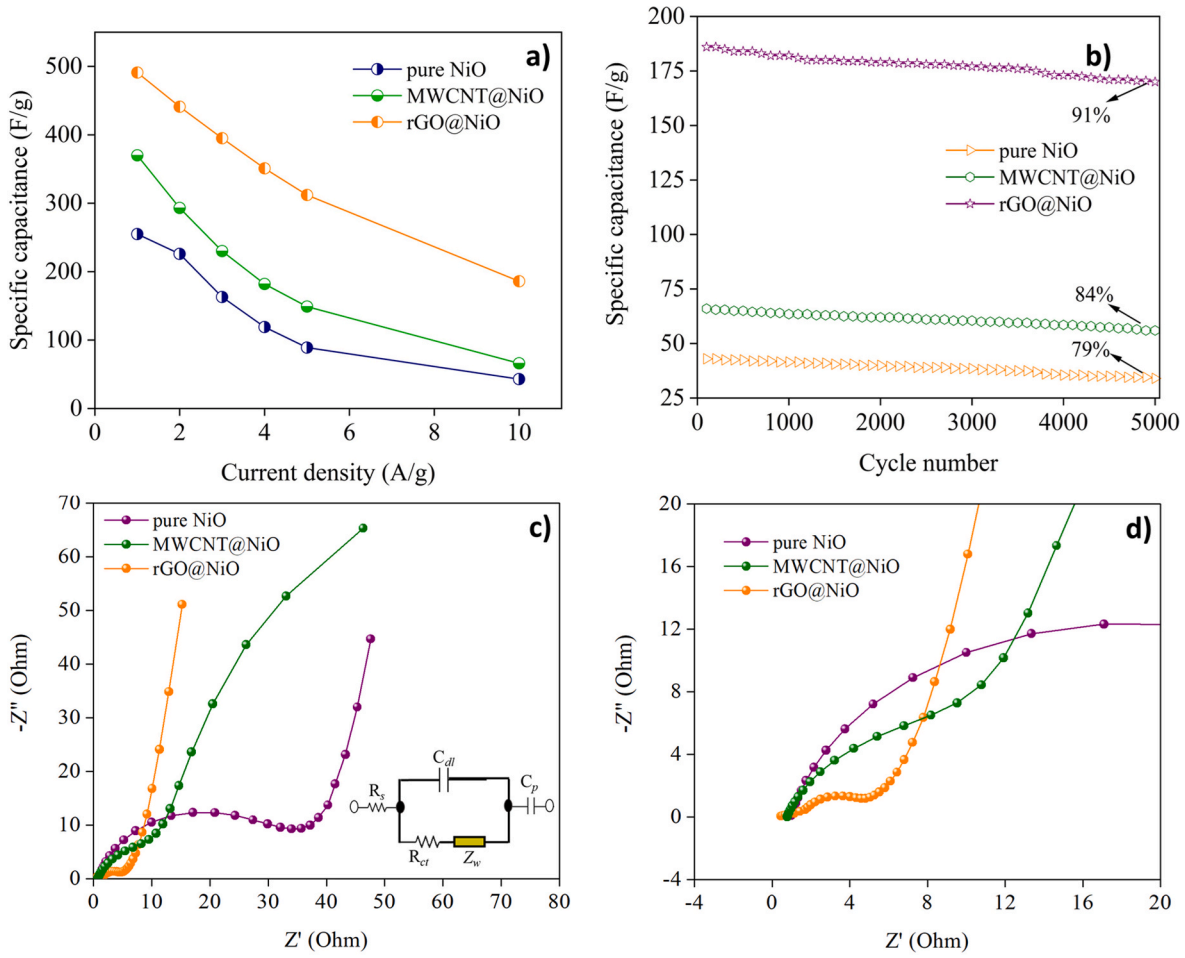

Fig. 12. (a) Specific capacitance at various current densities (b) Capacitance retention (5000 cycles at 10 A/g). (c) Nyquist plot with equivalent circuit and (d) Expanded Nyquist plots of the prepared samples as the working electrode.

Table 2
The specific capacitance of the prepared samples as the electrode at various current density.

Current density (A/g)	Specific capacitances C_{sp} (F/g)		
	pure NiO	MWCNT@NiO	rGO@NiO
1	255	370	491
2	226	293	441
3	163	230	395
4	119	182	351
5	89	149	312
10	43	66	186

storage capacity, leading to more efficient energy storage. rGO@NiO shows promise as an electrode for improved energy storage solutions due to its high charge capacity and low internal resistance.

We built an ASC device to explore the possible uses of the rGO@NiO electrodes. This device included negative and positive electrodes made of activated carbon (AC) and rGO@NiO. A separator separated these electrodes in a 1 M KOH solution, which served as the electrolyte. The schematic of the ASC device is shown in Fig. 13(a). Fig. 13(b) displays the CV curves of the rGO@NiO ASC device, taken at various scan speeds from 5 to 100 mV/s within a potential range of 0 to 1.2 V in the 1 M KOH electrolyte. The CV curves have a quasi-rectangular shape with strong redox peaks, indicating that the rGO@NiO electrode shows pseudocapacitive behavior. Additionally, the general shape of the CV curves stays consistent even at higher scan rates, showing little distortion. This behaviour suggests that the electrode material has excellent electrochemical reversibility and quick ion transport, indicating a good rate capability for applications that need high power. Fig. 13(c) presents the GCD curves of the rGO@NiO ASC device at different current densities ranging from 1 to 10 A/g within a 1.2 V voltage range. The symmetric and nearly linear triangular profiles suggest EDLC behaviour, which implies a capacitive charge storage mechanism primarily driven by electrostatic ion adsorption. The slight deviations from perfect linearity at higher current densities may reflect slight pseudocapacitive effects. The minor voltage drop (IR drop) observed at the beginning of each discharge curve shows that the rGO@NiO ASC device has low internal resistance.

Fig. 13(d) illustrates that the specific capacitance of the rGO@NiO ASC device varies with the current density. The specific capacitance was determined using the discharge curves. At current densities of 1, 2, 3, 4, 5, and 10 A/g, the device exhibits maximum specific capacitances of 159, 148, 78, 44, 33, and 26F/g, respectively. As the current density rises, the particular capacitance gradually decreases, which can be attributed to restricted ion diffusion and lower utilization of active sites at higher current rates [70]. Fig. 13(e) displays the cycling stability of the rGO@NiO ASC device after 5000 continuous charge–discharge cycles at a current density of 10 A/g. The specific capacitance dropped more during the first few cycles but stayed relatively stable throughout the experiment. After 5000 cycles, the device kept 94.3 % of its initial capacitance. This strong result highlights the durability and reversibility of the rGO@NiO electrode material during high-rate cycling. This demonstrates the device's efficiency and reversible charge storage capacity even after prolonged use. Fig. S3. (a) shows an AC impedance map for a rGO@NiO ASC device, with a frequency range of 0.01 to 100

Table 3
Summarizes the electrochemical measurements of nio/carbon electrodes published in previous research.

Samples	Preparation method	Electrolyte	Current density A/g	Specific capacitance F/g	Cycle life	Ref.
NiO-AC	Electrospinning	6 M KOH	1	248	98.2 % after 1000 cycles	[61]
NiO nanoflakes	Hydrothermal synthesis	2 M KOH	0.2	137.7	91.6 % after 1000 cycles	[62]
Porous MWCNTs–NiO composite	Soft template	2 M KOH	0.1	206	89 % after 200 cycles	[63]
NiO/CNTs	Microwave irradiation method	2 M KOH	1	258	86 % after 2500 cycles	[64]
RGO/CNT/NiO	Solvothermal process	6 M KOH	1	367	94 % after 1000 cycles	[65]
Porous nickel oxide–carbon nanotubes	Sonication	1 M KOH	1.11	245	64.3 % retention after 300 cycles	[66]
NiO nanoflakes/ graphene	Hydrothermal method	6 M KOH	5	240	100 % retention after 1500 cycles	[67]
NiO/rGO composite	one-pot chemical reduction method	6 M KOH	0.21	461	75 % retention after 5000 cycles	[68]
MWCNT@NiO	Microwave Synthesis	2 M KOH	1	370	84 % retention after 5000 cycles	Current study
rGO@NiO	Microwave Synthesis	2 M KOH	1	491	91 % retention after 5000 cycles	Current study

kHz and an amplitude of 5 mV. The rGO@NiO ASC device clearly demonstrates supercapacitor impedance characteristics. The equivalent series resistance (Rs) is measured at 1.05 Ω, indicating low internal resistance in the device. This low Rs value suggests excellent ionic conductivity of the electrolyte, good electrical contact between the active material and current collector, and high intrinsic conductivity of the rGO@NiO symmetric supercapacitor. Fig. S3. (b) also presents the Nyquist plots. The high-frequency region features a depressed semicircle, and a slightly curved transition area indicates low charge transfer resistance (Rct). This implies quick redox kinetics at the electrode–electrolyte interface, supported by the combined effect of rGO and NiO [78]. The rGO creates a conductive network, while NiO provides high pseudocapacitance through redox processes. Additionally, this image makes a 45° angle with the horizontal axis at low frequencies, indicating the involvement of diffusion-controlled charge storage [79]. Moreover, the XRD pattern of rGO@NiO on nickel foam after electrochemical tests, as shown in Fig. S4**,** demonstrates the structural integrity of the electrode material. The main diffraction peaks at 44.5°, 51.8°, and 76.4° (2θ) correspond to metallic nickel, linked to the nickel foam substrate below. NiO peaks at 37.2°, 43.3°, and 62.4°, representing (1 1 1), (2 0 0), and (2 2 0) planes, were also noted, confirming the presence of an fcc NiO phase. Moreover, rGO is likely absent due to its inferior crystalline structure or low concentration. When magnifying the 2θ angle from 35° to 70°, it can be seen that the NiO peaks appear with lower intensities compared to the Ni substrate peak but emerge after electrochemical cycling, providing evidence of NiO crystallinity and structural stability.

The energy and power densities of an rGO@NiO ASC device were calculated using below relations

$$E = \frac{1}{2 \times 3.6} CV^2 \tag{3}$$

$$P = \frac{E}{\Delta t} \times 3600 \tag{4}$$

where V is the applied voltage, C is the specific capacitance obtained from GCD, and Δt is the discharge time at the given current density. Fig. 13(f) shows the Ragone plot of the fabricated device's energy density (E) *vs* power density (P). The rGO@NiO ASC device achieved impressive energy densities of 31.92, 29.64, 15.618, 8.992, 6.606, and 5.208 Wh/kg, with power densities of 599.96, 1200.16, 1800.34, 2399.82, 3002.72, and 60009.23 W/kg. These values surpass those of previously published NiO-based supercapacitor systems, including NiO@Ni$(OH)_2$-*a*-MoO_3 (24 Wh/kg at 3100 W/kg) [71], NiO NSAs//graphene−CNT (8.8 Wh/kg at 4500 W/kg) [72], CNT@NiO//PCPs (25.4 Wh/kg at 400 W/kg) [73], NiO//AC (14.6 Wh/kg at 118 W/kg) [74], NiO-dots/Gh//AC (27.3 Wh/kg at 1562.6 W/kg) [75], NiO//AC (52.4 Wh/kg at 800 W/kg) [76], and rGO@NiO symmetric supercapacitor (47.8 Wh/kg at 545 W/kg) [77]. In addition, as shown in the inset of Fig. 13(f), two rGO@NiO ASC devices coupled in series can effectively light a green LED (3.0 V), indicating the practical feasibility of the fabricated rGO@NiO ASC device in energy storage applications.

Conclusion

We have successfully synthesized pure NiO, MWCNT@NiO, and rGO@NiO hybrid nanostructures via facile microwave-assisted synthesis. The electrochemical efficiency of the NiO was substantially enhanced by the addition of MWCNTs and rGO. The rGO@NiO nanostructures had a more active surface than pure NiO and MWCNT@NiO nanostructures, resulting in improved interface interaction within the material. rGO@NiO exhibited an exceptional cycling stability, retaining 91 % of its capacitance after 5000 cycles, and a remarkable specific capacitance of 491F/g at a current density of 1 A/g. This performance surpasses that of pure NiO and MWCNT@NiO. This can be attributed to the combined effects of the more active surface and high conductivity of rGO, along with NiO's electrochemical activity. Moreover, the rGO@NiO ASC device showed excellent energy and power density while maintaining stability during long-term cycling. These results suggest that rGO@NiO could be a promising option for practical energy storage in next-generation supercapacitor devices.

Declaration of Generative AI and AI-assisted technologies in the writing process:

During the preparation of this work, the authors used Grammerly to improve language and readability, with caution. After using this tool, the authors reviewed and edited the content as needed and takes full responsibility for the content of the publication.

Data availability

The data that support the findings of this study are available from the corresponding author upon reasonable request.

CRediT authorship contribution statement

Govindan Suresh Kumar: Writing – review & editing, Supervision, Validation, Formal analysis, Conceptualization. **Selvaraj Ranjith Priyan:** Visualization, Formal analysis, Writing – original draft, Investigation, Data curation. **Srinivasan Surendhiran:** Data curation, Formal analysis. **Srinivasan Ramalingam:** Resources, Data curation, Software, Formal analysis. **Raji Atchudan:** Software, Data curation, Visualization, Resources. **Nguyen Van Minh:** Visualization, Software,

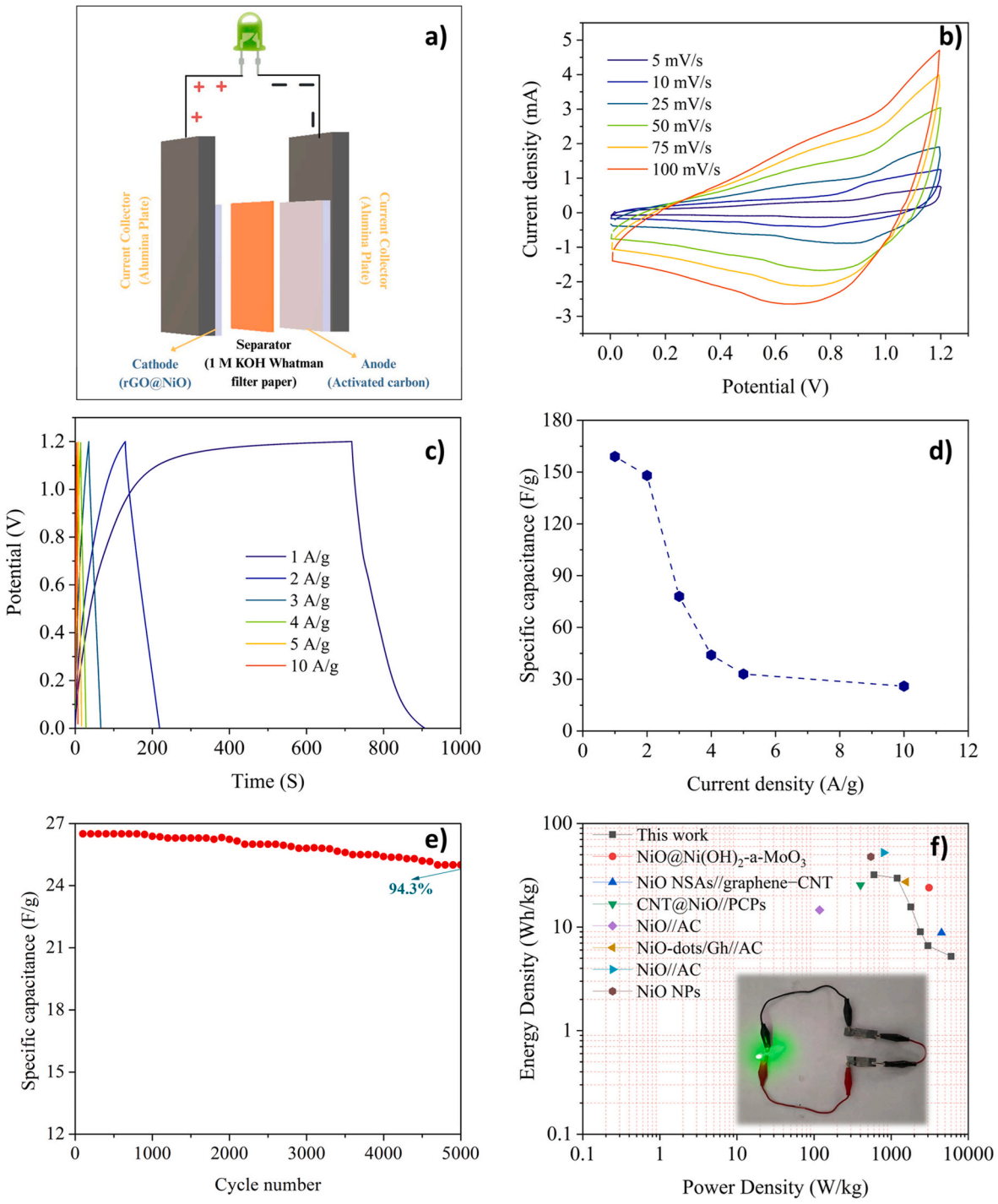

Fig. 13. (a) Schematic representation of the fabricated asymmetric supercapacitor. (b) CV curves of the asymmetric supercapacitor with various scan rates. (c) GCD curves of the asymmetric supercapacitor at different current densities. (d) variation of specific capacitance at different current densities. (e) Cycling stability at 10A/g (inset shows the last twenty-five cycles of the charge–discharge curves). (f) Ragone plots of the rGO@NiO asymmetric supercapacitor (Inset shows a photograph of the lighted LED by two asymmetric supercapacitors in series).

Data curation, Validation, Resources. **Mohammed Mujahid Alam:** Supervision, Writing – review & editing, Funding acquisition.

Declaration of competing interest

The authors declare that they have no known competing financial interests or personal relationships that could have appeared to influence the work reported in this paper.

Acknowledgments

The authors GSK and SRP express their gratitude to Dr. Shamima Hussain, UGC-DAE CSR, Kalpakkam for providing access to the FESEM facility. The authors extend their appreciation to University Higher Education Fund for funding this research work under Research Support Program for Central labs at King Khalid University through the project number CL/RP/4.

Appendix A. Supplementary material

Supplementary data to this article can be found online at https://doi.org/10.1016/j.jiec.2025.09.001.

References

[1] N. Poonam, K. Sharma, A. Arora, S.K. Tripathi, Review of supercapacitors: materials and devices, J. Storage Mater. 21 (2019) 801–825, https://doi.org/10.1016/j.est.2019.01.010.

[2] C. Duan, R.J. Kee, H. Zhu, C. Karakaya, Y. Chen, S. Ricote, A. Jarry, E.J. Crumlin, D. Hook, R. Braun, N.P. Sullivan, R. O'Hayre, Highly durable, coking and sulfur tolerant, fuel-flexible protonic ceramic fuel cells, Nature 557 (2018) 217–222, https://doi.org/10.1038/s41586-018-0082-6.

[3] K.M. Abraham, How comparable are sodium-ion batteries to lithium-ion counterparts, ACS Energy Lett. 5 (2020) 3544–3547, https://doi.org/10.1021/acsenergylett.0c02181.

[4] P. Wu, S. Cheng, M. Yao, L. Yang, Y. Zhu, P. Liu, O. Xing, J. Zhou, M. Wang, H. Luo, M. Liu, A. Low-Cost, Self-standing $NiCo_2O_4$@CNT/CNT multilayer electrode for flexible asymmetric solid-state supercapacitors, Adv. Funct. Mater. 27 (2017), https://doi.org/10.1002/adfm.201702160.

[5] Z. Zhang, Z. Zhang, X. Chen, H. Wang, H. Lu, Z. Shi, S. Feng, Metal–organic framework-derived hollow nanocubes as stable noble metal-free electrocatalyst for water splitting at high current density, CCS Chem. 6 (2023) 1324–1337, https://doi.org/10.31635/ccschem.023.202303256.

[6] L. Wang, X. Wang, J. Ouyang, Y. Guo, W. Xiong, L. Zhao, M. Li, Z. Hua, Z. Li, K. Du, C. Zhou, Y. Luo, Construction of polyaniline/MnO_2 core-shell nanocomposites in carbonized wood tracheids for high-performance all-solid-state asymmetric supercapacitors, Appl. Surf. Sci. 612 (2022) 155821, https://doi.org/10.1016/j.apsusc.2022.155821.

[7] J. Xu, Y. Sun, M. Lu, L. Wang, J. Zhang, J. Qian, X. Liu, Fabrication of hierarchical $MnMoO_4{\cdot}H_2O$@MnO_2 core-shell nanosheet arrays on nickel foam as an advanced electrode for asymmetric supercapacitors, Chem. Eng. J. 334 (2017) 1466–1476, https://doi.org/10.1016/j.cej.2017.11.085.

[8] L. Xia, H. Huang, Z. Fan, D. Hu, D. Zhang, A.S. Khan, M. Usman, L. Pan, Hierarchical macro-/meso-/microporous oxygen-doped carbon derived from sodium alginate: a cost-effective biomass material for binder-free supercapacitors, Mater. Des. 182 (2019) 108048, https://doi.org/10.1016/j.matdes.2019.108048.

[9] G.S. Gund, J.H. Park, R. Harpalsinh, M. Kota, J.H. Shin, T. Kim, Y. Gogotsi, H. S. Park, MXene/polymer hybrid materials for flexible AC-filtering electrochemical capacitors, Joule 3 (2019) 164–176, https://doi.org/10.1016/j.joule.2018.10.017.

[10] P. Nakhanivej, X. Yu, S.K. Park, S. Kim, J.-Y. Hong, H.J. Kim, W. Lee, J.Y. Hwang, J.E. Yang, C. Wolverton, J. Kong, M. Chhowalla, H.S. Park, Revealing molecular-level surface redox sites of controllably oxidized black phosphorus nanosheets, Nat. Mater. 18 (2018) 156–162, https://doi.org/10.1038/s41563-018-0230-2.

[11] R. Kumar, R. Matsuo, K. Kishida, M.M. Abdel-Galeil, Y. Suda, A. Matsuda, Homogeneous reduced graphene oxide supported NiO-MnO_2 ternary hybrids for electrode material with improved capacitive performance, Electrochim. Acta 303 (2019) 246–256, https://doi.org/10.1016/j.electacta.2019.02.084.

[12] X. Zhang, X. Li, F. Jiang, W. Du, C. Hou, Z. Xu, L. Zhu, Z. Wang, H. Liu, W. Zhou, H. Yuan, Improved electrochemical performance of 2D accordion-like MnV_2O_6 nanosheets as anode materials for Li-ion batteries, Dalton Trans. 49 (2020) 1794–1802, https://doi.org/10.1039/c9dt03845k.

[13] C. Xiong, B. Li, W. Dang, W. Zhao, C. Duan, L. Dai, Y. Ni, Co/CoS nanofibers with flower-like structure immobilized in carbonated porous wood as bifunctional material for high-performance supercapacitors and catalysts, Mater. Des. 195 (2020) 108942, https://doi.org/10.1016/j.matdes.2020.108942.

[14] S. Nisar, G. Dastgeer, M. Shahzadi, Z.M. Shahzad, E. Elahi, A. Irfan, J. Eom, H. Kim, D.-K. Kim, Gate-assisted $MoSe_2$ transistor to detect the streptavidin via supporter molecule engineering, Mater. Today Nano 24 (2023) 100405, https://doi.org/10.1016/j.mtnano.2023.100405.

[15] N. Duraisamy, A. Numan, S.O. Fatin, K. Ramesh, S. Ramesh, Facile sonochemical synthesis of nanostructured NiO with different particle sizes and its electrochemical properties for supercapacitor application, J. Colloid Interf. Sci. 471 (2016) 136–144, ISSN 0021-9797. https://doi.org/10.1016/j.jcis.2016.03.013.

[16] B. Bhujun, M.T.T. Tan, A.S. Shanmugam, Study of mixed ternary transition metal ferrites as potential electrodes for supercapacitor applications, Results Phys. 7 (2016) 345–353, https://doi.org/10.1016/j.rinp.2016.04.010.

[17] Y. Zhang, L. Li, H. Su, W. Huang, X. Dong, Binary metal oxide: advanced energy storage materials in supercapacitors, J. Mater. Chem. A 3 (2014) 43–59, https://doi.org/10.1039/c4ta04996a.

[18] S. Ci, Z. Wen, Y. Qian, S. Mao, S. Cui, J. Chen, NiO-microflower formed by nanowire-weaving nanosheets with interconnected ni-network decoration as supercapacitor electrode, Sci. Rep. 5 (2015), https://doi.org/10.1038/srep11919.

[19] M.B. Askari, P. Salarizadeh, M.T.T. Moghadam, S. Azizi, M.H.R. Zadeh, Binary transition metal oxide/carbon compounds-based electrode materials for supercapacitor application: a comprehensive review, J. Alloy. Compd. (2025) 180573, https://doi.org/10.1016/j.jallcom.2025.180573.

[20] M.B. Askari, M.T.T. Moghadam, P. Salarizadeh, Three-component NiO/Fe_3O_4/rGO nanostructure as an electrode material towards supercapacitor and alcohol electrooxidation, Heliyon 10 (2024) e39399, https://doi.org/10.1016/j.heliyon.2024.e39399.

[21] M.B. Askari, P. Salarizadeh, M.H.R. Zadeh, MoO_3/WO_3/rGO as electrode material for supercapacitor and catalyst for methanol and ethanol electrooxidation, Sci. Rep. 14 (2024), https://doi.org/10.1038/s41598-024-59018-2.

[22] S. Chand, R. Kumar, N. Thakur, K. Kumar, A. Umar, T. Almas, S. Baskoutas, Sustainable synthesis and multifunctional applications of biowaste-derived carbon nanomaterials and metal oxide composites: a review, Chemosphere 385 (2025) 144540, https://doi.org/10.1016/j.chemosphere.2025.144540.

[23] P. Salarizadeh, M.B. Askari, H. Beydaghi, M. Rastgoo-Deylami, S.M. Rozati, Hybrid of cerium dioxide nanoparticles/reduced graphene oxide as an electrode material for supercapacitor applications, J. Phys. Chem. Solid 159 (2021) 110284, https://doi.org/10.1016/j.jpcs.2021.110284.

[24] M.M. Sk, C.Y. Yue, K. Ghosh, R.K. Jena, Review on advances in porous nanostructured nickel oxides and their composite electrodes for high-performance supercapacitors, J. Power Sources 308 (2016) 121–140, https://doi.org/10.1016/j.jpowsour.2016.01.056.

[25] S. Kostromin, M. Asandulesa, A. Podshivalov, S. Bronnikov, Effect of rGO:MWCNTs ratio on electrical conductivity of polyazomethine/rGO:MWCNTs nanocomposites, Mater. Res. Express 6 (2019) 115053, https://doi.org/10.1088/2053-1591/ab46f8.

[26] J. Xu, L. Wu, Y. Liu, J. Zhang, J. Liu, S. Shu, X. Kang, Q. Song, D. Liu, F. Huang, Y. Hu, NiO-rGO composite for supercapacitor electrode, Surf. Interfaces 18 (2019) 100420, https://doi.org/10.1016/j.surfin.2019.100420.

[27] G.S. Gund, D.P. Dubal, S.S. Shinde, C.D. Lokhande, Architectured morphologies of chemically prepared NiO/MWCNTs nanohybrid thin films for high performance supercapacitors, ACS Appl. Mater. Interf. 6 (2014) 3176–3188, https://doi.org/10.1021/am404422g.

[28] M. Pathak, S.M. Jeong, C.S. Rout, Graphene hybrids for supercapacitor applications, Chem. Commun. (2025), https://doi.org/10.1039/d4cc06809b.

[29] J. Jose, J. Vigneshwaran, A. Baby, R. Viswanathan, S.P. Jose, S.P. B, Dimensionally engineered ternary nanocomposite of reduced graphene oxide/multiwalled carbon nanotubes/zirconium oxide for supercapacitors, J. Alloy. Compd. 896 (2021) 163067, https://doi.org/10.1016/j.jallcom.2021.163067.

[30] S.D. Dhas, P.S. Maldar, M.D. Patil, M.R. Waikar, R.G. Sonkawade, A.V. Moholkar, Sol-gel synthesized nickel oxide nanostructures on nickel foam and nickel mesh for a targeted energy storage application, J. Storage Mater. 47 (2021) 103658, https://doi.org/10.1016/j.est.2021.103658.

[31] J. Xu, M. Wang, Y. Liu, J. Li, H. Cui, One-pot solvothermal synthesis of size-controlled NiO nanoparticles, Adv. Powder Technol. 30 (2019) 861–868, https://doi.org/10.1016/j.apt.2019.01.016.

[32] J.E. Nady, A. Shokry, M. Khalil, S. Ebrahim, A.M. Elshaer, M. Anas, One-step electrodeposition of a polypyrrole/NiO nanocomposite as a supercapacitor electrode, Sci. Rep. 12 (2022), https://doi.org/10.1038/s41598-022-07483-y.

[33] C. Wang, J. Xu, M. Yuen, J. Zhang, Y. Li, X. Chen, W. Zhang, Hierarchical composite electrodes of nickel oxide nanoflake 3D graphene for high-performance pseudocapacitors, Adv. Funct. Mater. 24 (2014) 6372–6380, https://doi.org/10.1002/adfm.201401216.

[34] M. Hakamada, T. Abe, M. Mabuchi, Electrodes from carbon nanotubes/NiO nanocomposites synthesized in modified watts bath for supercapacitors, J. Power Sources 325 (2016) 670–674, https://doi.org/10.1016/j.jpowsour.2016.06.091.

[35] D.S. Hall, D.J. Lockwood, C. Bock, B.R. MacDougall, Nickel hydroxides and related materials: a review of their structures, synthesis and properties, Proc. Royal Soc. Math. Phys. Eng. Sci. 471 (2014) 20140792, https://doi.org/10.1098/rspa.2014.0792.

[36] S.H. Jhung, T. Jin, Y.K. Hwang, J. Chang, Microwave effect in the fast synthesis of microporous materials: which stage between nucleation and crystal growth is accelerated by microwave irradiation? Chem. A Eur. J. 13 (2007) 4410–4417, https://doi.org/10.1002/chem.200700098.

[37] S.R. Priyan, G.S. Kumar, S. Surendhiran, Mohd. Shkir, Size-controlled synthesis of mesoporous silica nanoparticles using rice husk by microwave-assisted sol–gel method, Int. J. Appl. Ceram. Technol. 20 (2023) 2807–2816, https://doi.org/10.1111/ijac.14444.

[38] L. Clausen, I. Fabricius, B.E.T. Measurements, Outgassing of minerals, J. Colloid Interf. Sci. 227 (2000) 7–15, https://doi.org/10.1006/jcis.2000.6880.

[39] B. Zhao, H. Zhuang, T. Fang, Z. Jiao, R. Liu, X. Ling, B. Lu, Y. Jiang, Self-assembly of NiO/graphene with three-dimension hierarchical structure as high performance electrode material for supercapacitors, J. Alloy. Compd. 597 (2014) 291–298, https://doi.org/10.1016/j.jallcom.2014.01.192.

[40] R. Kumar, A. Soam, V. Sahajwalla, Sucrose-derived carbon-coated nickel oxide (SDCC-NiO) as an electrode material for supercapacitor applications, Mater. Adv. 1 (2020) 609–616, https://doi.org/10.1039/d0ma00323a.

[41] N.A. Jawad, K.H. Hassan, Structural characterization of nio nanoparticles prepared by green chemistry synthesis using arundo donaxi leaves extract, J. Phys. Conf. Ser. 1818 (2021) 012007, https://doi.org/10.1088/1742-6596/1818/1/012007.

[42] Z. Wu, X. Wang, S.H.K. Annamareddy, S. Gao, Q. Xu, H. Algadi, D. Sridhar, P. Wasnik, B.B. Xu, L. Weng, Z. Guo, Dielectric properties and thermal conductivity of polyvinylidene fluoride synergistically enhanced with silica@multi-walled carbon nanotubes and boron nitride, ES Mater. Manuf. (2023), https://doi.org/10.30919/esmm5f847.

[43] Y. Zhang, Y. Shen, X. Xie, W. Du, L. Kang, Y. Wang, X. Sun, Z. Li, B. Wang, One-step synthesis of the reduced graphene oxide@NiO composites for supercapacitor electrodes by electrode-assisted plasma electrolysis, Mater. Des. 196 (2020) 109111, https://doi.org/10.1016/j.matdes.2020.109111.

[44] G.A. Babu, G. Ravi, T. Mahalingam, M. Kumaresavanji, Y. Hayakawa, Influence of microwave power on the preparation of NiO nanoflakes for enhanced magnetic and supercapacitor applications, Dalton Trans. 44 (2015) 4485–4497, https://doi.org/10.1039/c4dt03483j.

[45] I.T. Bello, K.O. Otun, G. Nyongombe, O. Adedokun, G.L. Kabongo, M.S. Dhlamini, Non-modulated synthesis of cobalt-doped MoS_2 for improved supercapacitor performance, Int. J. Energy Res. 46 (2022) 8908–8918, https://doi.org/10.1002/er.7765.

[46] Mu. Naushad, T. Ahamad, M. Ubaidullah, J. Ahmed, A.A. Ghafar, K.M. Al-Sheetan, P. Arunachalam, Nitrogen-doped carbon quantum dots (N-CQDs)/Co_3O_4 nanocomposite for high performance supercapacitor, J. King Saud. Univ. Sci. 33 (2020) 101252, https://doi.org/10.1016/j.jksus.2020.101252.

[47] V.G. Baldovino-Medrano, V. Niño-Celis, R.I. Giraldo, Systematic analysis of the nitrogen adsorption–desorption isotherms recorded for a series of materials based on microporous–mesoporous amorphous aluminosilicates using classical methods, J. Chem. Eng. Data 68 (2023) 2512–2528, https://doi.org/10.1021/acs.jced.3c00257.

[48] G. Meng, Q. Yang, X. Wu, P. Wan, Y. Li, X. Lei, X. Sun, J. Liu, Hierarchical mesoporous NiO nanoarrays with ultrahigh capacitance for aqueous hybrid supercapacitor, Nano Energy 30 (2016) 831–839, https://doi.org/10.1016/j.nanoen.2016.09.012.

[49] P. Shen, H. Zhang, S. Zhang, L. Fei, Fabrication of completely interface-engineered $Ni(OH)_2$/rGO nanoarchitectures for high-performance asymmetric supercapacitors, Appl. Surf. Sci. 460 (2017) 65–73, https://doi.org/10.1016/j.apsusc.2017.09.145.

[50] A.K. Mondal, D. Su, S. Chen, A. Ung, H. Kim, G. Wang, Mesoporous $MnCo_2O_4$ with a flake-like structure as advanced electrode materials for lithium-ion batteries and supercapacitors, Chem. A Eur. J. 21 (2014) 1526–1532, https://doi.org/10.1002/chem.201405698.

[51] H.T. Das, K. Mahendraprabhu, T. Maiyalagan, P. Elumalai, Performance of solid-state hybrid energy-storage device using reduced graphene-oxide anchored sol-gel derived Ni/NiO nanocomposite, Sci. Rep. 7 (2017), https://doi.org/10.1038/s41598-017-15444-z.

[52] J. Liu, J. Wang, C. Xu, H. Jiang, C. Li, L. Zhang, J. Lin, Z.X. Shen, advanced energy storage devices: basic principles, analytical methods, and rational materials design, Adv. Sci. 5 (2018) 1700322, https://doi.org/10.1002/advs.418.

[53] T. Brezesinski, J. Wang, S.H. Tolbert, B. Dunn, Ordered mesoporous α-MOO_3 with iso-oriented nanocrystalline walls for thin-film pseudocapacitors, Nat. Mater. 9 (2010) 146–151, https://doi.org/10.1038/nmat2612.

[54] T.-C. Liu, W.G. Pell, B.E. Conway, S.L. Roberson, Behavior of molybdenum nitrides as materials for electrochemical capacitors: comparison with ruthenium oxide, J. Electrochem. Soc. 145 (1998) 1882–1888, https://doi.org/10.1149/1.1838571.

[55] A. Iakunkov, V. Skrypnychuk, A. Nordenström, E.A. Shilayeva, M. Korobov, M. Prodana, M. Enachescu, S.H. Larsson, A. VTalyzin, Activated graphene as a material for supercapacitor electrodes: effects of surface area, pore size distribution and hydrophilicity, PCCP 21 (2019) 17901–17912, https://doi.org/10.1039/c9cp03327k.

[56] D. Shrestha, Evaluation of physical and electrochemical performances of hardwood and softwood derived activated carbons for supercapacitor application, Mater. Sci. Energy Technol. 5 (2022) 353–365, https://doi.org/10.1016/j.mset.2022.09.002.

[57] S.R. Priyan, G.S. Kumar, R. Rajendran, G. Arumugam, N. Van Minh, M.M. Alam, Microwave-assisted sol-gel synthesis of MFe_2O_4@SiO_2 (M = Cu, Ni, Co) ceramic nanostructures using rice husk as a sustainable precursor for electrochemical energy storage, Ceram. Int. (2024), https://doi.org/10.1016/j.ceramint.2024.09.095.

[58] R. Kumar, R.K. Singh, R. Savu, P.K. Dubey, P. Kumar, S.A. Moshkalev, Microwave-assisted synthesis of void-induced graphene-wrapped nickel oxide hybrids for supercapacitor applications, RSC Adv. 6 (2016) 26612–26620, https://doi.org/10.1039/c6ra00426a.

[59] S. Gadipelli, J. Guo, Z. Li, C.A. Howard, Y. Liang, H. Zhang, P.R. Shearing, D.J. L. Brett, Understanding and optimizing capacitance performance in reduced graphene-oxide based supercapacitors, Small Methods 7 (2023), https://doi.org/10.1002/smtd.202201557.

[60] A. Shah, S. Senapati, H.C.A. Murthy, L.R. Singh, M. Mahato, Supercapacitor performance of NiO, NiO-MWCNT, and NiO–Fe-MWCNT composites, ACS Omega 8 (2023) 33380–33391, https://doi.org/10.1021/acsomega.3c03044.

[61] M.S. Kolathodi, M. Palei, T.S. Natarajan, Electrospun NiO nanofibers as cathode materials for high performance asymmetric supercapacitors, J. Mater. Chem. A 3 (2015) 7513–7522, https://doi.org/10.1039/c4ta07075e.

[62] Y.-Z. Zheng, H.-Y. Ding, M.-L. Zhang, Preparation and electrochemical properties of nickel oxide as a supercapacitor electrode material, Mater. Res. Bull. 44 (2008) 403–407, https://doi.org/10.1016/j.materresbull.2008.05.002.

[63] Y. Zheng, M. Zhang, P. Gao, Preparation and electrochemical properties of multiwalled carbon nanotubes–nickel oxide porous composite for supercapacitors, Mater. Res. Bull. 42 (2007) 1740–1747, https://doi.org/10.1016/j.materresbull.2006.11.022.

[64] V. Sannasi, K.U. Maheswari, C. Karthikeyan, S. Karuppuchamy, H_2O_2-assisted microwave synthesis of NiO/CNT nanocomposite material for supercapacitor applications, Ionics 26 (2020) 4067–4079, https://doi.org/10.1007/s11581-020-03563-z.

[65] R. Rajendran, L.K. Shrestha, R.M. Kumar, R. Jayavel, J.P. Hill, K. Ariga, Composite nanoarchitectonics for ternary systems of reduced graphene oxide/carbon nanotubes/nickel oxide with enhanced electrochemical capacitor performance, J. Inorg. Organomet. Polym Mater. 25 (2014) 267–274, https://doi.org/10.1007/s10904-014-0102-4.

[66] A.D. Su, X. Zhang, A. Rinaldi, S.T. Nguyen, H. Liu, Z. Lei, L. Lu, H.M. Duong, Hierarchical porous nickel oxide–carbon nanotubes as advanced pseudocapacitor materials for supercapacitors, Chem. Phys. Lett. 561–562 (2013) 68–73, https://doi.org/10.1016/j.cplett.2013.01.023.

[67] Y.-G. Zhu, G.-S. Cao, C.-Y. Sun, J. Xie, S.-Y. Liu, T.-J. Zhu, X.B. Zhao, H.Y. Yang, Design and synthesis of NiO nanoflakes/graphene nanocomposite as high performance electrodes of pseudocapacitor, RSC Adv. 3 (2013) 19409, https://doi.org/10.1039/c3ra42091d.

[68] Y. Bu, S. Wang, H. Jin, W. Zhang, J. Lin, J. Wang, Synthesis of porous NiO/reduced graphene oxide composites for supercapacitors, J. Electrochem. Soc. 159 (2012) A990–A994, https://doi.org/10.1149/2.036207jes.

[69] K.A. Kumar, K. Subalakshmi, J. Senthilselvan, Effect of mixed valence state of titanium on reduced recombination for natural dye-sensitized solar cell applications, J. Solid State Electrochem. 20 (2016) 1921–1932, https://doi.org/10.1007/s10008-016-3191-x.

[70] R. Wali, K. Moulaee, M. Qasymeh, R. Maalej, G. Neri, Atomic layer deposition of NiO-coated CNT nanocomposites: tailoring electrochemical properties for salivary lactate detection, J. Electroanal. Chem. 971 (2024) 118594.

[71] G. Manibalan, Y. Govindaraj, J. Yesuraj, P. Kuppusami, G. Murugadoss, R. Murugavel, M.R. Kumar, Facile synthesis of NiO@$Ni(OH)_2$-α-MoO_3 nanocomposite for enhanced solid-state symmetric supercapacitor application, J. Colloid Interf. Sci. 585 (2020) 505–518, https://doi.org/10.1016/j.jcis.2020.10.032.

[72] A.R. Rashid, A.G. Abid, S. Manzoor, A. Mera, T.I. Al-Muhimeed, A.A. AlObaid, S. N. Shah, M.N. Ashiq, M. Imran, M. Najam-Ul-Haq, Inductive effect in Mn-doped ZnO nanoribon arrays grown on Ni foam: a promising key for boosted capacitive and high specific energy supercapacitors, Ceram. Int. 47 (2021) 28338–28347, https://doi.org/10.1016/j.ceramint.2021.06.251.

[73] H. Yi, H. Wang, Y. Jing, T. Peng, Y. Wang, J. Guo, Q. He, Z. Guo, X. Wang, Advanced asymmetric supercapacitors based on CNT@$Ni(OH)_2$ core–shell composites and 3D graphene networks, J. Mater. Chem. A 3 (2015) 19545–19555, https://doi.org/10.1039/c5ta06174a.

[74] F. Yu, L. Zhu, T. You, F. Wang, Z. Wen, Preparation of chestnut-like porous NiO nanospheres as electrodes for supercapacitors, RSC Adv. 5 (2015) 96165–96169, https://doi.org/10.1039/c5ra17122a.

[75] M. Jing, C. Wang, H. Hou, Z. Wu, Y. Zhu, Y. Yang, X. Jia, Y. Zhang, X. Ji, Ultrafine nickel oxide quantum dots enbedded with few-layer exfoliative graphene for an asymmetric supercapacitor: enhanced capacitances by alternating voltage, J. Power Sources 298 (2015) 241–248, https://doi.org/10.1016/j.jpowsour.2015.08.039.

[76] R. Vinodh, R.S. Babu, R. Atchudan, H.-J. Kim, M. Yi, L.M. Samyn, A.L.F. De Barros, Fabrication of high-performance asymmetric supercapacitor consists of nickel oxide and activated carbon (NIO//AC), Catalysts 12 (2022) 375, https://doi.org/10.3390/catal12040375.

[77] M. Bulla, V. Kumar, R. Devi, S. Kumar, A.K. Sisodiya, R. Dahiya, A.K. Mishra, Natural resource-derived NiO nanoparticles via aloe vera for high-performance symmetric supercapacitor, Sci. Rep. 14 (2024), https://doi.org/10.1038/s41598-024-57606-w.

[78] B. Rani, N.K. Sahu, Electrochemical properties of $CoFe_2O_4$ nanoparticles and its rGO composite for supercapacitor, Diam. Relat. Mater. 108 (2020) 107978, https://doi.org/10.1016/j.diamond.2020.107978.

[79] R.C. Ambare, B.J. Lokhande, Solution concentration and decomposition temperature dependent electrochemical behavior of aqueous route spray pyrolysed Mn_3O_4: supercapacitive approach, J. Mater. Sci. Mater. Electron. 28 (2017) 12246–12252, https://doi.org/10.1007/s10854-017-7040-1.